Progress in Physics of Applied Materials 2 (2022) 183–194

Semnan University

Progress in Physics of Applied Materials

journal homepage: https://ppam.semnan.ac.ir/

Effect of precursor on physical properties and photocatalytic activity of 2D g-C_3N_4 nanosheets

N. Memarian[a]*, E. Farahi[a], N. Tobeiha[a], I. Concina[b]

[a] *Faculty of Physics, Semnan University, P.O. Box: 35195-363, Semnan, Iran*
[b] *Department of Engineering Sciences and Mathematics, Luleå University of Technology, 97187 Luleå, Sweden*

ARTICLE INFO

Article history:
Received: 17 December 2022
Revised: 30 December 2022
Accepted: 31 December 2022

Keywords:
Graphitic carbon nitride
Photocatalyst
RhB dye degradation
different precursor

ABSTRACT

2-dimensional graphitic carbon nitride (g-C_3N_4) has specific properties that makes it a desirable candidate for extensive applications. This work provides a systematic study for choosing precursors to prepare g-C_3N_4 with tailored characteristics. g-C_3N_4 samples have been prepared by thermal decomposition of different precursors (i.e., melamine, urea, and thiourea). Various characterization techniques such as SEM, EDS, XRD, DRS, BET, and FTIR have been used to determine the physical properties of the prepared samples. SEM analysis showed nanoflake and nanosheet structures with no elemental impurity in EDS analysis. Furthermore, FTIR analysis confirmed the formation of graphitic carbon nitride structure. BET results showed a significant enhancement of specific surface area by a factor of 2.8 for the sample prepared with urea precursor. The photocatalytic activity for rhodamine B (RhB) degradation is also presented. The results revealed that urea-based g-C_3N_4 could be a promising candidate for photocatalytic applications due to its appropriate physical properties and highest dye removal.

1. Introduction

As the global energy crisis and environmental pollution are two of the most pressing challenges for human society, the need to develop alternative means of generating energy and eliminating pollutants has steadily increased [1]. In recent years, extensive efforts have been made to develop high-efficiency photocatalysts: their capability of exploiting solar light to promote useful chemical reaction has been indeed proved important in several environmental applications [2, 3]. Photocatalysts can indeed be used for hydrogen production, CO_2 reduction, ammonia synthesis and degradation of pollutants.

Since the Wang Group first discovered metal-free graphite carbon nitride (g-C_3N_4) compound in 2009[4], g-C_3N_4 has become a promising candidate for photocatalytic applications. g-C_3N_4 is a non-metallic, polymeric semiconductor material composed of carbon and nitrogen, which possesses a stacked two dimensional (2D) layered structure. The electronic properties and morphology can be tuned to improve the photocatalytic activity of g-C_3N_4 for different applications, including water splitting and H_2 generation, removal of dyes from water, CO_2 conversion and N_2 fixation [1, 5-7].

Different methods, such as thermal polycondensation, physical and chemical vapor deposition, solvothermal synthesis and microwave heating [3, 5], have been used for the preparation of g-C_3N_4. In addition, other synthesis strategies [8], including the ionothermal synthesis (molten salt strategy) [9], molecular self-assembly [10], microwave irradiation [11], and ionic liquid strategy [12] have been successfully applied. The most common method for preparation of g- C_3N_4 is the thermal decomposition of different nitrogen-rich precursors or monomers such as urea [13, 14], dicyandiamide [15-17], melamine [18-20], cyanamide [21, 22], and thiourea [23, 24]. Zhu et al.[25] studied the isoelectric point of g-C_3N_4 prepared from three different precursors (i.e., melamine, thiourea, and urea) at 550°C. Zeta potential tests showed that the sample prepared from urea possessed the highest isoelectric point and exhibited the best methylene blue adsorption activity. In another study, Fang et al.[26] investigated the photocatalytic degradation of Rhodamine B (RhB) by g-

* Corresponding author.
E-mail address: n.memarian@semnan.ac.ir

DOI: 10.22075/ppam.2022.29345.1049

C_3N_4, under both visible and UV light irradiation. It was found that the oxygen superoxide radical (O_2) is the predominant reactive oxygen species (ROS) in degrading RhB.

In the present work, g-C_3N_4 two-dimensional nanosheets were prepared by direct heating (polymerization) method using different precursors, namely urea; thiourea and melamine whose effect on the chemical, physical, and functional properties of g-C_3N_4 were investigated.

2. Experimental

Urea, thiourea, and melamine were used as precursors for synthesis of g-C_3N_4. All reagents were purchased from Merck and used directly without any further purification. In each experiment 3 gr of precursor were put into an alumina crucible and then heated at 500°C in a muffle furnace for 2h at a heating rate of 3˚/min. Eventually, the material was cooled to room temperature at a cooling rate of 5˚/min, and the yellow colored substance g-C_3N_4 was labeled as U500, T500, M500 for urea, thiourea, and melamine precursors, respectively.

To investigate the morphology of the samples, field emission scanning electron microscopy (FESEM) analysis was carried out on a MIRA3 TESCAN instrument. The samples were coated with Au to promote conduction. The elemental composition of the samples was determined using energy dispersive X-ray spectroscopy (EDS) in the FESEM. The crystalline phase structure was detected by X-ray diffraction (XRD) analysis (Advance Bruker D-8) with CuKα radiation with λ=1.54 Å from 10°-80° and the resolution of 0.065 degree. The Fourier transform infrared (FTIR) spectra of the samples (embedded in KBr pellets) were obtained using 8400S-SHIMAZU spectrometer. The nitrogen (N_2) adsorption-desorption isotherms of the samples were recorded using a BELSORP-mini instrument, to find out the specific surface area and the pore size distribution of as-prepared samples by Brunauer–Emmet–Teller (BET) and Barrett-Jonyer-Halenda (BJH) methods, respectively. UV-Vis-NIR diffuse reflectance spectra (DRS) of the samples were measured by an Avantes AvaSpec 3648 spectrophotometer.

Photocatalytic activity of the g-C_3N_4 samples was evaluated by studying the degradation of Rhodamine B (RhB). The absorption spectra were recorded using a PerkinElmer, Lambda 25 spectrophotometer to evaluate the degradation of RhB. In each experiment 5 mg of the catalyst was added into 50 mL of RhB (10 ppm) aqueous solution. Before irradiation, the reaction mixture remained under dark for 30 min to reach the adsorption/desorption equilibrium. The photocatalytic experiments were performed under a mercury-lamp (50 W) irradiation. At certain time intervals, 3 ml of the solution were taken out and centrifuged. The absorption spectrum of the solution was then monitored.

3. Results and discussion

The microstructure and morphology of the samples are presented in Figure 1. All the samples, irrespective of the precursor used, show the presence of nanoparticles smaller than 20 nm clustered together to form a seemingly porous over-structure. Moreover, all samples display a laminar structure and nanosheets are formed. However, for M500 (Fig. 1(a)) the sheets are closely packed indicating the presence of fewer pores in the structure. For U500 sample (Fig. 1(c)) the over-structures are clearly separated and the nanosheets are clearly recognizable, which could affect other physical properties specially the active surface area of this sample.

EDS spectra of g-C_3N_4 samples are shown in Figure 2. The presence of Au characteristic peak is due to the Au coating for FESEM analysis. C/N ratio was similar for the samples M500 and T500 (0.59), which is lower than the ideal ratio for g-C_3N_4 (0.75). This low value could be related to the abundance of amino groups or carbon vacancy[18]. On the contrary, sample U500 showed a C/N ratio as high as 0.92, indicating a higher amount of carbon and a decrease of nitrogen in the structure.

The XRD patterns of g-C_3N_4 samples are shown in Figure 3. The peak located at around 2θ=27.5˚, indexed as the (002) peak, is attributed to the repeat structure of in-plate and the interlayer stacking of stratified (layered) structure[27]. A stronger (002) peak for M500 is shown to be related to the inter-planar spacing between the g-C_3N_4 layers, indicating that the material contains a heptazine ring on the g-C_3N_4 lattice structure[28]. A very small shift to higher degrees, from 27.24° to 27.53° is observed for M500 sample. This shift indicates a decrease in inter-planar spacing from 0.327 nm for U500 and 0.325 for T500 to 0.324 nm for M500. Hence, M500 has more densely packed g-C_3N_4 layers, which has been reported to improve the charge transfer among the layers[18]. In addition, the crystallite size of the samples has been calculated by Debye–Scherrer equation[29-31]. The calculated crystallite sizes are 8.8, 7.1, and 3.0 nm for M500, T500, and U500, respectively.

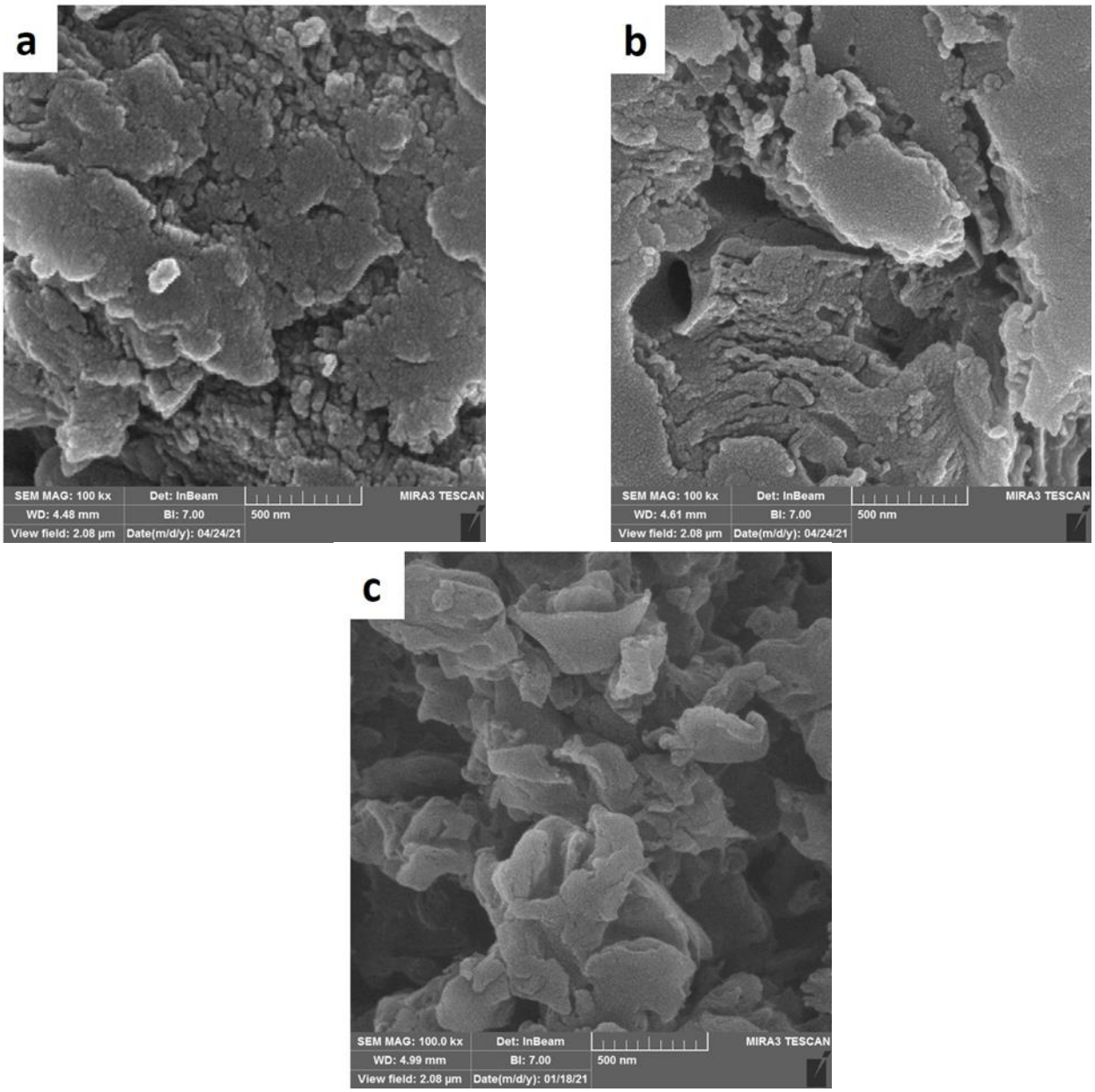

Fig. 1. FESEM images of g-C_3N_4 samples: (a) M500, (b) T500, (c) U500.

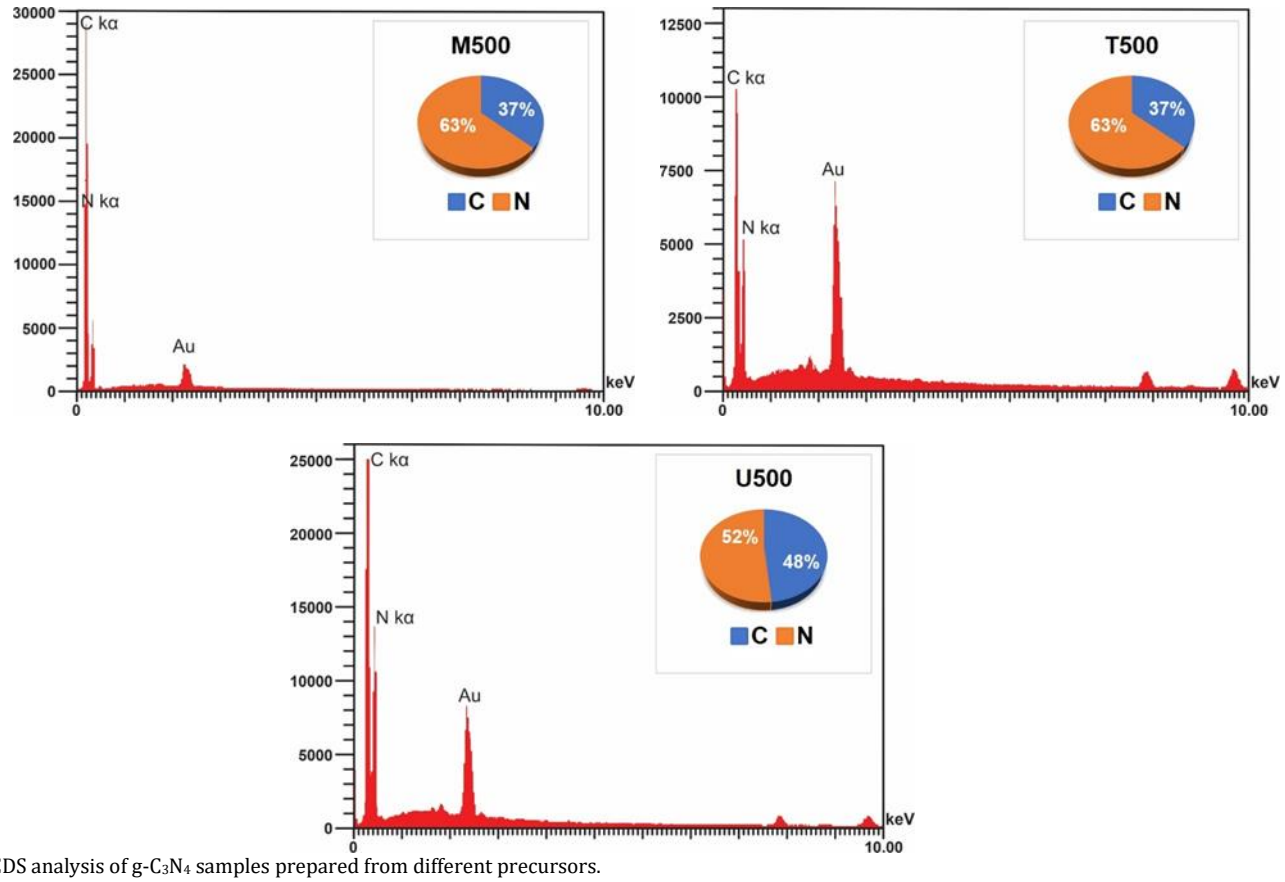

Fig. 2. EDS analysis of g-C_3N_4 samples prepared from different precursors.

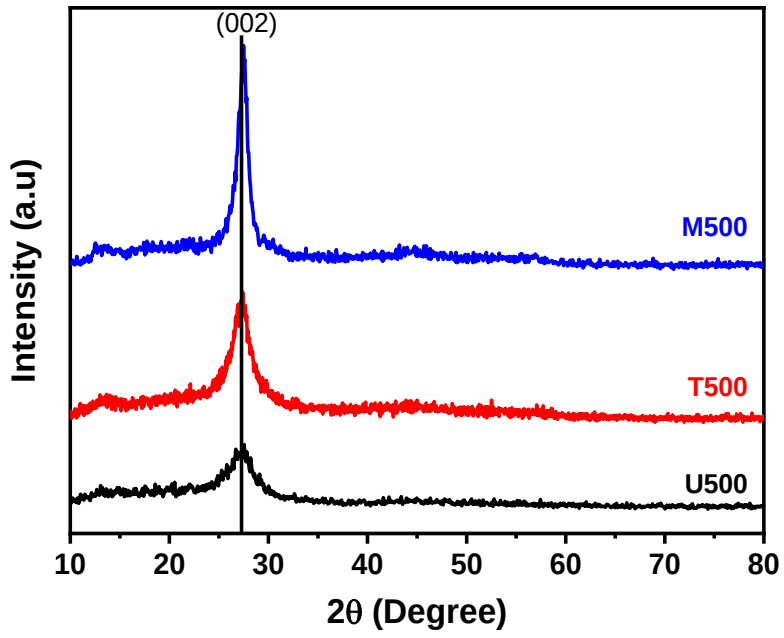

Fig. 3. XRD patterns of g-C_3N_4 nanosheets from different precursors.

Table 1. Comparison between the ratio of main vibrations for heptazine and vibrations of non-condensed amino groups in the analyzed samples.

	M500	T500	U500
Ratio breathing mode heptazine/N-H stretching	3.0	5.6	4.0

The chemical bonding and functional groups of produced g-C_3N_4 were investigated by FTIR spectroscopy (Fig. 4). All the samples displayed the characteristic vibrations associated to the presence of heptazine rings, confirming its formation during the synthesis. Specifically, a strong absorption peak, located at 810 cm^{-1}, was found in

all the samples, which corresponds to the tri-s-triazine ring breathing mode [24, 32].

In addition, the broad band located in the interval 1658-1200 cm^{-1} relates to the stretching modes of C-N heterocycles[33]. This band arises from the overlapping of unresolved peaks, rather well visible in the samples T500 and U500. In particular, peaks at 1660, 1565, and 1416 cm^{-1} are the characteristics of the stretching vibrational modes of heptazine-derived repeating units. In addition, peaks at 1320 and 1244 cm^{-1} are related to the out-of-plane bending vibrations of heptazine rings[8, 34]. However, these absorption modes are not possible to discriminate in M500 sample, suggesting a lower intensity for these vibration in this sample, probably due to the closer packing identified in the XRD analysis.

The condensation of amino groups resulted incomplete in all the samples, as testified by the broad bands around 3200 cm^{-1} (N-H stretching mode of primary amines) [24, 33].

Further proof of a partial condensation of amine groups is a weak absorption band located around 880 cm^{-1}, visible in all the samples under investigation, which is also attributed to vibrational modes of N-H bonds [8], indicating an incomplete condensation of amino groups.

The comparison of the area of this vibration with that of the peak attributed to the breathing mode of tri-s-triazine rings (810 cm^{-1}) resulted in different ratios for different samples (see Table 1).

This analysis highlighted that thiourea-derived g-C_3N_4 featured the lowest amount of un-condensed amino groups, while the sample prepared from melamine showed the best result in this respect, with the best condensation rate of the batch.

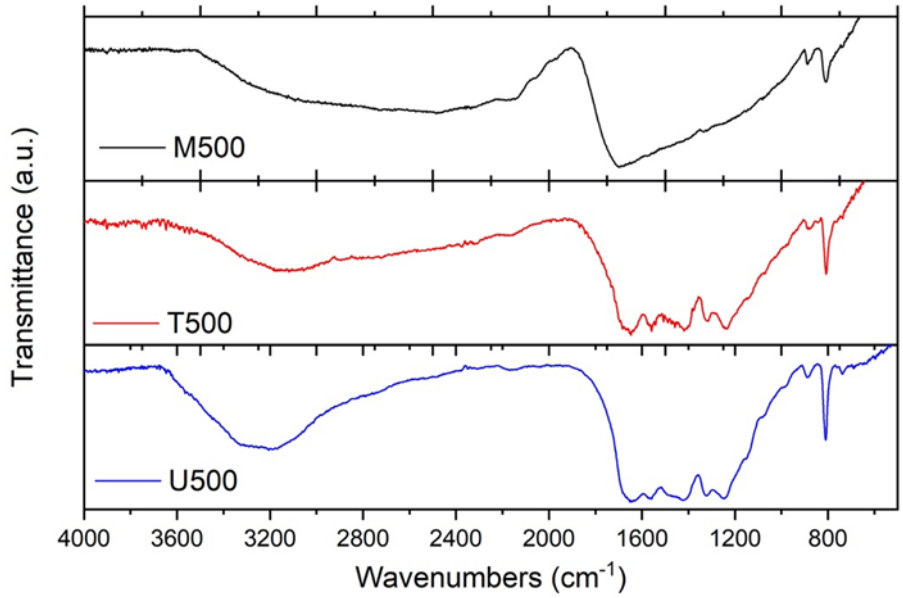

Fig. 4. FTIR spectra of different g-C_3N_4 nanopowders.

The sorption–desorption isotherms and pore size distribution curves of the samples are shown in Figure 5. All the samples clearly showed hysteresis loop characteristic of type IV isotherm, with H3 hysteresis loop[35, 36], indicating the mesoporous structure, along with slit-like pores due to the presence of plate-like aggregates[33, 37], consistent with FESEM results. The pore size distributions of all three samples were found spread over a wide range of 2-50 nm, confirming the mesoporous nature of the materials. These pores could contribute in providing efficient and appropriate active sites for dye absorption and photocatalytic reactions.

The surface area, total pore volume, and average pore size of the samples were calculated from BET and BJH methods and are listed in Table 2. The results revealed significant differences in the sample batch. Indeed, the specific surface area of U500 was found to be almost 10 times higher than the specific surface area of T500 and 4.8 times higher than that of M500. Furthermore, the average pore size of U500 and M500 was approximately the same, while it was larger for the sample prepared from thiourea. However, the total pore volume of U500 was 4.23 times and 5.79 times larger than that of M500 and T500, respectively. The results indicated that U500 had the largest surface area and the highest total pore volume, potentially making it the most suitable material among the ones herein investigated to perform as photocatalyst. Indeed, these features should promote an enhanced dye adsorption, which is critical asset in catalysis.

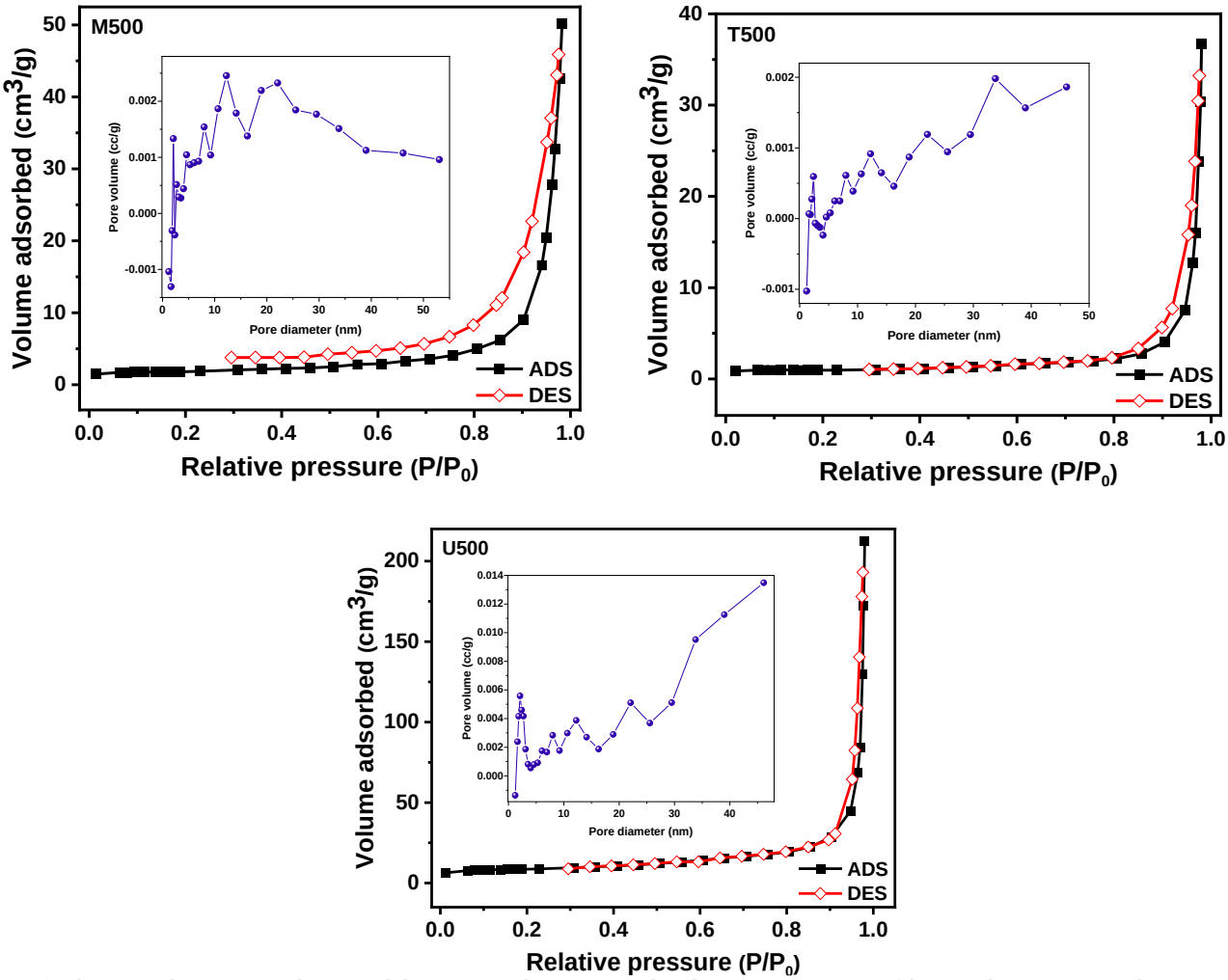

Fig. 5. Adsorption-desorption isotherms and the corresponding pore size distribution curves (inset) of the nanosheet g-C_3N_4 powders.

Table 2. Specific surface area, total pore volume, and average pore size as determined from BET analysis.

Sample	Specific surface area (m^2/g)	Total pore volume (cm^3/g)	Average pore size (nm)
M500	7.0021	0.0776	44.33
T500	3.8499	0.056737	58.95
U500	32.361	0.3287	40.63

Another relevant feature in photocatalysis is how the catalytic material responds to irradiation. We then carried out diffuse reflectance spectroscopy (the spectra are reported in Fig. 6(a)) to investigate how the g-C_3N_4 samples obtained from different precursors interact with light and to uncover possible differences among them. DRS analysis showed a similar behavior in terms of light reflectance for all the analyzed samples in the range 800-600 nm. From 600 nm to 400 nm, the sample M500 displayed the best light absorption of the batch, while from 400 nm to 200 nm the sample prepared from urea featured a more significant absorption (about 90%) compared to the other materials. Some investigations reported indirect band gap [24, 25, 38-40] for g-C_3N_4, others reported direct band gap [41, 42], and some reported both direct and indirect band gaps [43]. In this work both direct and indirect band gaps of g-C_3N_4 samples have been calculated from DRS analysis by using the Kubelka-Munk method as follows [40, 44]:

$$F(R)=\frac{(1-R)^2}{2R} \quad (1)$$

Where F(R) is the Kubelka-Munk function, which is proportional to the absorption coefficient (α) of samples

and R is the reflectance of sample. Then by using Tauc's equation (Eq. 2) and then extrapolating the linear part of curve to the x axis (energy, $h\upsilon$), the band gap energy (Eg) would be determined[38, 45].

$$\alpha \times h\upsilon = B(h\upsilon - E_g)^n \quad (2)$$

Where B is a constant. The exponent "n" is 1/2 for the direct and 2 for the indirect allowed transitions. Tauc plot calculations for direct and indirect band gaps are presented in Figures 6 (b) and (c), respectively.

The direct band gap of samples was found to be in the range of 2.84 to 2.92 eV. In addition, indirect band gap of samples was calculated between 2.33 to 2.78 eV. The results showed the highest band gap belongs to the sample prepared from melamine reagent, and the lowest band gap belongs to the sample prepared from thiourea.

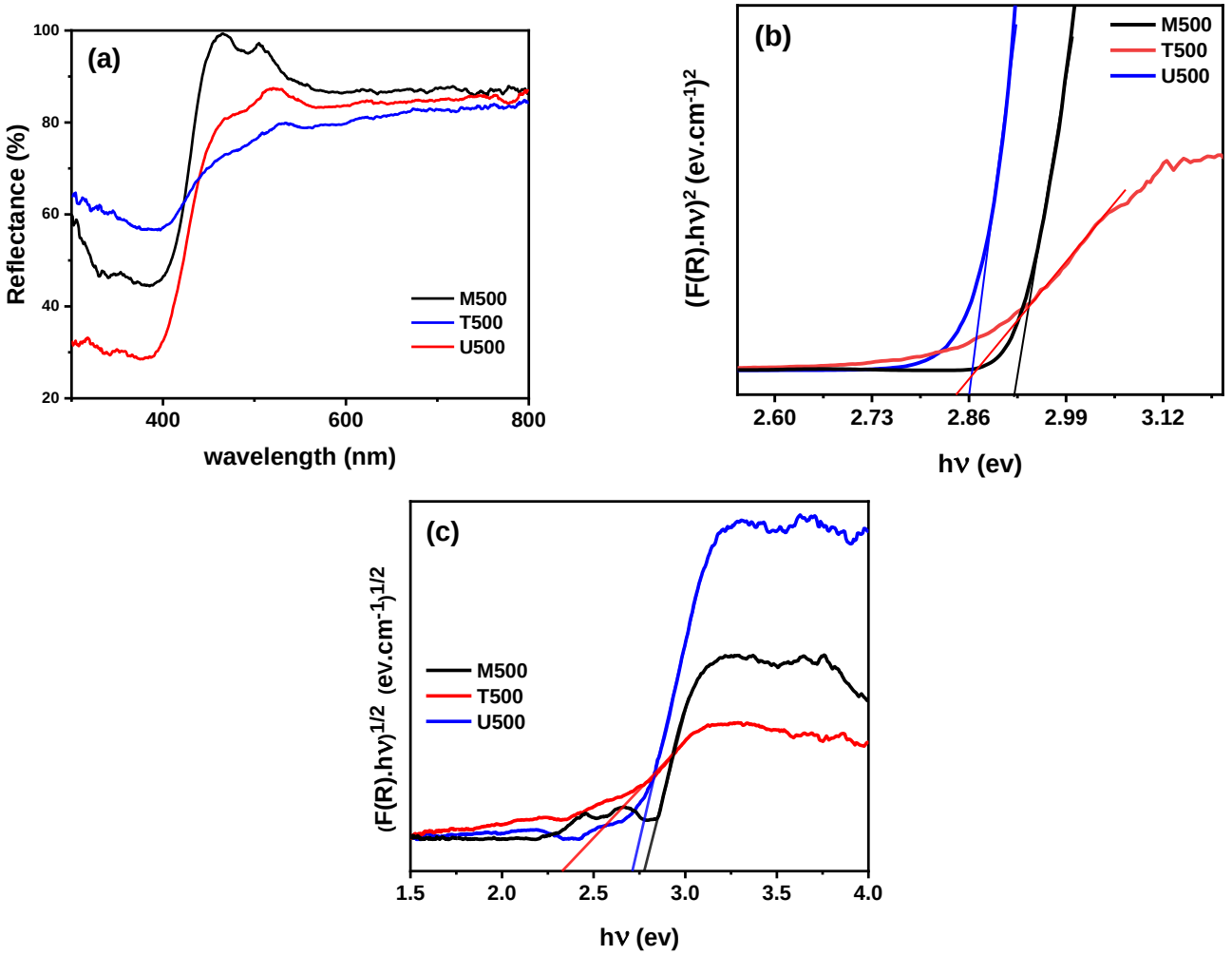

Fig. 6. DRS analysis (a) reflectance spectra of samples, (b) direct band gap Tauc plot calculation, (c) indirect band gap Tauc plot calculation.

Photocatalytic activity of the prepared g-C_3N_4 nanosheets was studied by analyzing the decomposition of RhB dye. Prior to light irradiation, the reaction mixture was left under dark for 30 min, aimed at reaching the adsorption-desorption equilibrium. No relevant adsorption of RhB molecules was observed, even at higher duration times (data not shown).

Fig. 7 (a, b, and c) shows the optical adsorption spectra of the RhB solutions subjected to degradation upon light irradiation using the samples M500, T500, and U500. The degradation percentage was calculated by using the following equation[46, 47]:

$$DE(\%) = \frac{C_0 - C}{C_0} \times 100 \quad (3)$$

Where C_0 and C are the dye concentrations at t=0 and after different irradiation time, respectively. Quite similar performance, in terms of degradation capability, was observed for the three materials under investigation (Fig. 7 c): after 3 hours under irradiation samples M500 and T500 degraded about 40% of the initial RhB amount, while a slightly better catalytic ability was shown by the sample U500, prepared from urea (50% of RhB was removed after 3 hours). It should be noted that no hypsochromic shift of the absorption peak centered at 554 nm was observed. This shift was often reported in literature and attributed to the N-deethylation of rhodamine B to rhodamine during the catalytic reactions [48]. The absence of this shift strongly suggests that another degradation path is active in the present case. On the other hand, the analysis of reaction kinetics (presented in Fig. 8) did not reveal a pseudo-first order kinetics, as often reported in literature for the same

reaction catalyzed by semiconductors. Indeed, the reaction course is well fitted by an exponential function ($y = y_0 + A_1 e^{\left(\frac{x}{t_1}\right)}$) for samples M500 and U500, indicating a reaction order higher than one. As for sample T500, the reaction course is better fitted by a sigmoid function ($y = A_2 + \frac{(A_1 - A_2)}{\left(1+\left(\frac{x}{x_0}\right)^p\right)}$): this trend is associated to an autocatalytic reaction [49], indicating that a different mechanism is at work.

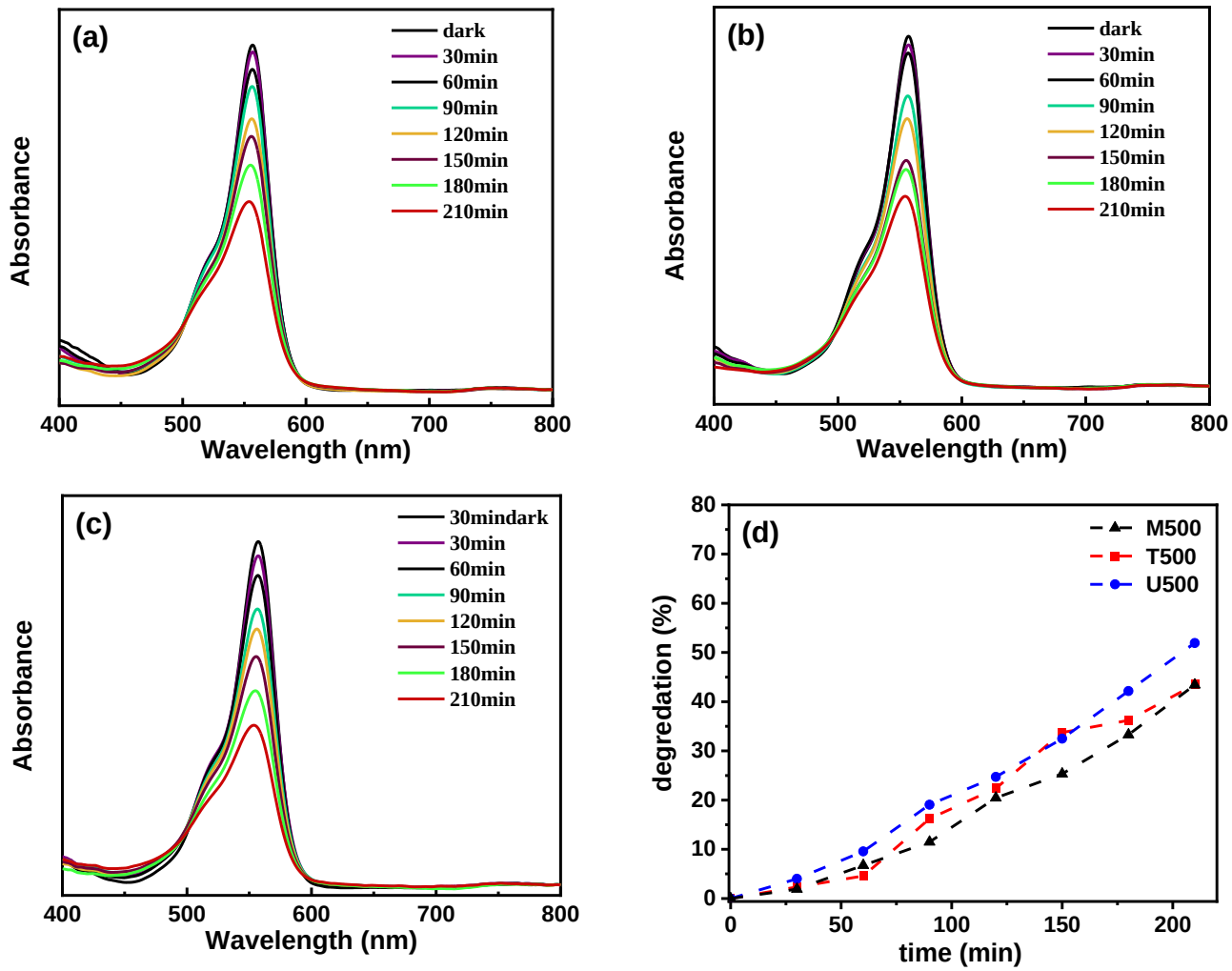

Fig. 7. Absorption spectra of RhB solution with (a) M500, (b) T500, and (c) U500 as photocatalyst. (d) RhB photocatalytic degradation results of three catalysts.

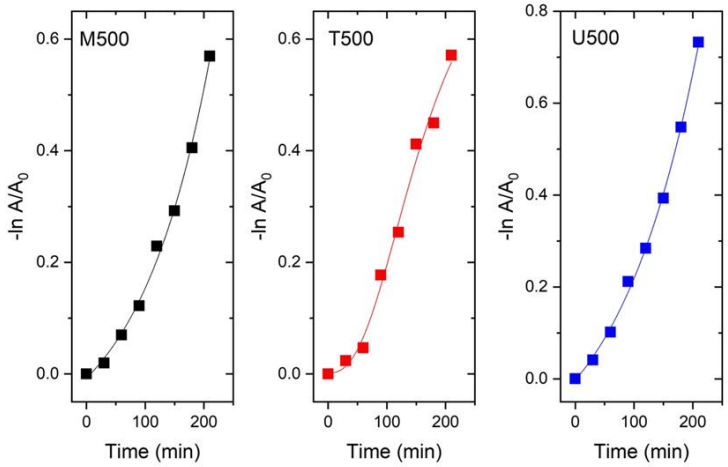

Fig. 8. analysis of the reaction courses for the RhB degradation supported by the materials under investigation. Markers are experimental points; lines are fitting functions.

Table 3. Fitting parameters for RhB catalytic degradation and apparent kinetic constants for the degradation of rhodamine B catalyzed by the g-C_3N_4 materials under investigation.

Sample	Fitting equation	Fitting parameters	Apparent kinetic constant (min^{-1} x 10^3)
M500	Exponential growth	y_0 = -0.13993 A_1 = 0.1323 t_1 = 125.51071 R^2 = 0.99653	7.97
T500	Logistic	A_1 = 0.0016 A_2 = 0.85783 x_0 = 163.70768 p = 2.49845 R^2 = 0.99078	17.7
U500	Exponential growth	y_0 = -0.22114 A_1 = 0.21813 t_1 = 142.68663 R^2 = 0.99766	7.01

Generally, the photocatalytic mechanism for dye degradation starts with the absorption of incident photons and excitation of electrons from valance band to conduction band. The generation of electron-hole pairs in semiconductor catalyst and the subsequent photodegradation of dye are depicted as follow [46, 50]:

$$g\text{-}C_3N_4 + h\nu \rightarrow e^- + h^+ \quad (4)$$

$$O_2 + e^- \rightarrow O_2^{*-} \quad (5)$$

$$H_2O \rightarrow OH^- + H^+ \quad (6)$$

$$OH^- + h^+ \rightarrow {}^*OH \quad (7)$$

$$O_2^{*-} + H^+ \rightarrow HO_2^* \quad (8)$$

$$HO_2^* + e^- \rightarrow HO_2^- \quad (9)$$

$$HO_2^- + H^+ \rightarrow H_2O_2 \quad (10)$$

$$H_2O_2 + e^- \rightarrow {}^*OH + OH^- \quad (11)$$

$$\text{Pollutant} + {}^*OH \rightarrow \text{degradation product} \quad (12)$$

$$\text{Pollutant} + h^+ \rightarrow \text{oxidation product} \quad (13)$$

$$\text{Pollutant} + e^- \rightarrow \text{reduction product} \quad (14)$$

Recently, Ashiq et al.[51] revealed by radical trapping experiment that in photocatalytic dye degradation mechanism of RhB using g-C_3N_4/Ag@$CoWO_4$ Z-scheme composite the OH• radicals are the dominant reactive species for dye degradation. Superoxide radicals O_2^-• and the holes may indirectly help the dye degradation by reacting with H_2O/OH^- to generate extra OH• radicals.

We eventually analyzed the degradation percentage and apparent kinetic constants as a function of the physical and chemical features of the samples under investigation (the results are shown in Fig. 9).

The capability of degrading RhB was found to depend on some physical characteristics of the materials: the crystallite sizes (the smaller the size the better the degradation), the surface area (the higher the area the better the performance), the total pore volume (the higher the volume the better the degradation). These results are somehow expected and the design of a good catalyst should take them all into account. The chemical composition, in terms of carbon content, also plays a role: a higher carbon content seems promoting a higher RhB degradation (Fig. 9 (d)). This might be due to a better ability of carbon atoms to bind the RhB molecules by using their oxygens, for which the nitrogen has less affinity. On the other hand, the degree of un-condensed amino group was found to be neutral in photocatalyst.

The apparent kinetic constant was harder to analyze: we could identify only a dependence on the average pore size (Fig. 9 (e)), while all the other physical and chemical features appeared not to influence it. The higher the pore size, the faster the reaction: it was also unexpected to find an excellent exponential trend (R^2=0.99997) linking the reaction rate with the average pore size. At this point we can only speculate about the reason behind this finding: the higher the average pore size, the easier the flow of RhB molecules through them (in and out).

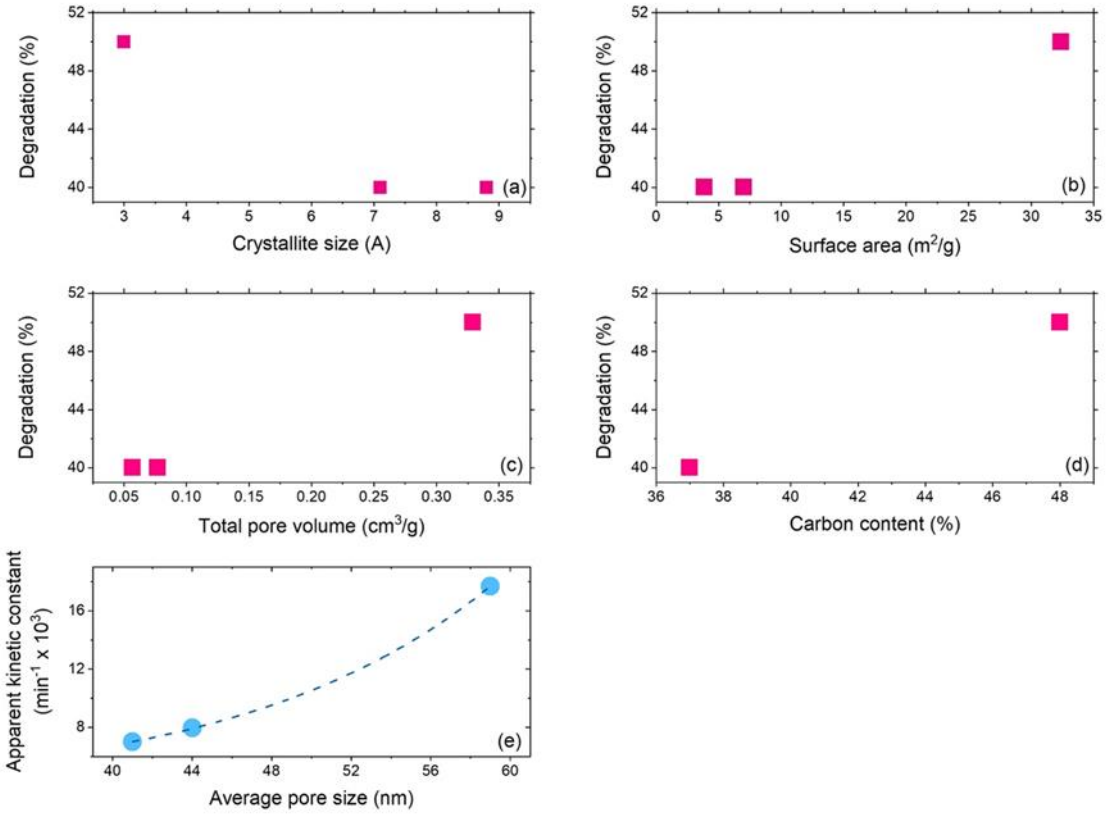

Fig. 9. Dependece of degradation percentage (a-d) and apparent kinetc constant (e) on relevant physical and chemical features of the catalysts.

4. Conclusion

To sum up, 2D g-C_3N_4 nanosheets have been synthesized by thermal condensation (polymerization) of three different precursors. FESEM and XRD results confirms the formation of 2D layered structure of samples. The band gap of obtained nanosheets is suitable for photocatalytic purposes, such as dye removal from water. It was shown that the physical and chemical properties of g-C_3N_4 are affected by the precursors and were explored here. The photocatalytic skills of the prepared materials were evaluated for the degradation of RhB: while the observed performance was not excellent in terms of degradation percentage, we could find some interesting correlation between the catalytic outcomes and the chemical and physical features of the investigated materials, which are worth further investigation.

Declaration of competing interest:

The authors have no competing interests to declare that are relevant to the content of this article.

References

[1] A. Kumar, P. Raizada, A. Hosseini-Bandegharaei, V.K. Thakur, V.-H. Nguyen, P. Singh, "C-, N-Vacancy defect engineered polymeric carbon nitride towards photocatalysis: viewpoints and challenges." Journal of Materials Chemistry A 9 (2021) 111-153.

[2] H. Jung, T.-T. Pham, E.W. Shin, "Interactions between ZnO nanoparticles and amorphous g-C_3N_4 nanosheets in thermal formation of g-C_3N_4/ZnO composite materials: The annealing temperature effect." Applied Surface Science 458 (2018) 369-381.

[3] B. Rhimi, C. Wang, D.W. Bahnemann, "Latest progress in g-C_3N_4 based heterojunctions for hydrogen production via photocatalytic water splitting: a mini review." Journal of Physics: Energy 2 (2020) 042003.

[4] X. Wang, K. Maeda, A. Thomas, K. Takanabe, G. Xin, J.M. Carlsson, K. Domen, M. Antonietti, "A metal-free polymeric photocatalyst for hydrogen production from water under visible light." Nature materials 8 (2009) 76-80.

[5] J. Wang, S. Wang, "A critical review on graphitic carbon nitride (g-C_3N_4)-based materials: Preparation, modification and environmental application." Coordination Chemistry Reviews 453 (2022) 214338.

[6] L. Bai, H. Huang, S. Yu, D. Zhang, H. Huang, Y. Zhang, "Role of transition metal oxides in g-C_3N_4-based heterojunctions for photocatalysis and supercapacitors." Journal of Energy Chemistry 64 (2022) 214-235.

[7] G. Nabi, N. Malik, W. Raza, "Degradation effect of temperature variation and dye loading g-C_3N_4 towards organic dyes." Inorganic Chemistry Communications 119 (2020) 108050.

[8] J. Wena, J. Xie, X. Chen, X. Li, "A review on g-C_3N_4-based photocatalysts." Applied Surface Science 391 (2017) 72-123.

[9] W.r. Lee, Y.S. Jun, J. Park, G.D. Stucky, "Crystalline poly (triazine imide) based g-CN as an efficient electrocatalyst for counter electrodes of dye-sensitized solar cells using a triiodide/iodide redox electrolyte." Journal of Materials Chemistry A 3 (2015) 24232-24236.

[10] Y. Ishida, L. Chabanne, M. Antonietti, M. Shalom, "Morphology control and photocatalysis enhancement by the one-pot synthesis of carbon nitride from preorganized hydrogen-bonded supramolecular precursors." Langmuir 30 (2014) 447-451.

[11] L. Lin, P. Ye, C. Cao, Q. Jin, G.-S. Xu, Y.-H. Shen, Y.-P. Yuan, "Rapid microwave-assisted green production of a crystalline polyimide for enhanced visible-light-induced photocatalytic hydrogen production." Journal of Materials Chemistry A 3 (2015) 10205-10208.

[12] L. Xu, S. Ling, H. Li, P. Yan, J. Xia, J. Qiu, K. Wang, H. Li, S. Yuan, "Photoelectrochemical monitoring of 4-chlorophenol by plasmonic Au/graphitic carbon nitride composites." Sensors and Actuators B: Chemical 240 (2017) 308-314.

[13] Z. Zhang, D. Jiang, D. Li, M. He, M. Chen, "Construction of $SnNb_2O_6$ nanosheet/g-C_3N_4 nanosheet two-dimensional heterostructures with improved photocatalytic activity: synergistic effect and mechanism insight." Applied Catalysis B: Environmental 183 (2016) 113-123.

[14] J. Wen, J. Xie, H. Zhang, A. Zhang, Y. Liu, X. Chen, X. Li, "Constructing multifunctional metallic Ni interface layers in the g-C_3N_4 nanosheets/amorphous NiS heterojunctions for efficient photocatalytic H_2 generation." ACS Applied Materials & Interfaces 9 (2017) 14031-14042.

[15] M. Zhang, J. Xu, R. Zong, Y. Zhu, "Enhancement of visible light photocatalytic activities via porous structure of g-C_3N_4." Applied Catalysis B: Environmental 147 (2014) 229-235.

[16] F. Li, P. Zhu, S. Wang, X. Xu, Z. Zhou, C. Wu, "One-pot construction of Cu and O co-doped porous g-C_3N_4 with enhanced photocatalytic performance towards the degradation of levofloxacin." RSC advances 9 (2019) 20633-20642.

[17] L. Yang, X. Liu, Z. Liu, C. Wang, G. Liu, Q. Li, X. Feng, "Enhanced photocatalytic activity of g-C_3N_4 2D nanosheets through thermal exfoliation using dicyandiamide as precursor." Ceramics International 44 (2018) 20613-20619.

[18] Q. Xu, D. Ma, S. Yang, Z. Tian, B. Cheng, J. Fan, "Novel g-C_3N_4/g-C_3N_4 S-scheme isotype heterojunction for improved photocatalytic hydrogen generation." Applied Surface Science 495 (2019) 143555.

[19] S. Vignesh, S. Chandrasekaran, M. Srinivasan, R. Anbarasan, R. Perumalsamy, E. Arumugam, M. Shkir, H. Algarni, S. AlFaify, "TiO_2-CeO_2/g-C_3N_4 S-scheme heterostructure composite for enhanced photo-degradation and hydrogen evolution performance with combined experimental and DFT study." Chemosphere 288 (2022) 132611.

[20] S. Cao, Q. Huang, B. Zhu, J. Yu, "Trace-level phosphorus and sodium co-doping of g-C_3N_4 for enhanced photocatalytic H_2 production." Journal of Power Sources 351 (2017) 151-159.

[21] Y. Shiraishi, Y. Kofuji, H. Sakamoto, S. Tanaka, S. Ichikawa, T. Hirai, "Effects of surface defects on photocatalytic H_2O_2 production by mesoporous graphitic carbon nitride under visible light irradiation." ACS Catalysis 5 (2015) 3058-3066.

[22] L. Liang, Y. Cong, F. Wang, L. Yao, L. Shi, "Hydrothermal pre-treatment induced cyanamide to prepare porous g-C_3N_4 with boosted photocatalytic performance." Diamond and Related Materials 98 (2019) 107499.

[23] J. Xiao, Y. Xie, F. Nawaz, Y. Wang, P. Du, H. Cao, "Dramatic coupling of visible light with ozone on honeycomb-like porous g-C_3N_4 towards superior oxidation of water pollutants." Applied Catalysis B: Environmental 183 (2016) 417-425.

[24] Y. Hong, E. Liu, J. Shi, X. Lin, L. Sheng, M. Zhang, L. Wang, J. Chen, "A direct one-step synthesis of ultrathin g-C_3N_4 nanosheets from thiourea for boosting solar photocatalytic H_2 evolution." international journal of hydrogen energy 44 (2019) 7194-7204.

[25] B. Zhu, P. Xia, W. Ho, J. Yu, "Isoelectric point and adsorption activity of porous g-C_3N_4." Applied Surface Science 344 (2015) 188-195.

[26] S. Fang, K. Lv, Q. Li, H. Ye, D. Du, M. Li, "Effect of acid on the photocatalytic degradation of rhodamine B over g-C_3N_4." Applied Surface Science 358 (2015) 336-342.

[27] Z. Zhu, H. Pan, M. Murugananthan, J. Gong, Y. Zhang, "Visible light-driven photocatalytically active g-C_3N_4 material for enhanced generation of H_2O_2." Applied Catalysis B: Environmental 232 (2018) 19-25.

[28] J. Oh, J.M. Lee, Y. Yoo, J. Kim, S.-J. Hwang, S. Park, "New insight of the photocatalytic behaviors of graphitic carbon nitrides for hydrogen evolution and their associations with grain size, porosity, and photophysical properties." Applied Catalysis B: Environmental 218 (2017) 349-358.

[29] A. Mohammad, M.E. Khan, M.H. Cho, T. Yoon, "Fabrication of binary SnO_2/TiO_2 nanocomposites under a sonication-assisted approach: Tuning of band-gap and water depollution applications under visible light irradiation." Ceramics International 47 (2021) 15073-15081.

[30] D. Hernández-Uresti, D. Sanchez-Martinez, L. Torres-Martinez, "Novel visible light-driven $PbMoO_4$/g-C_3N_4 hybrid composite with enhanced photocatalytic performance." Journal of Photochemistry and Photobiology A: Chemistry 345 (2017) 21-26.

[31] M. Banari, N. Memarian, "Effect of the seed layer on the UV photodetection properties of ZnO nanorods." Materials Science and Engineering: B 272 (2021) 115332.

[32] T. Paul, D. Das, B.K. Das, S. Sarkar, S. Maiti, K.K. Chattopadhyay, "$CsPbBrCl_2$/g-C_3N_4 type II

heterojunction as efficient visible range photocatalyst." Journal of hazardous materials 380 (2019) 120855.
[33] H. Wang, Z. Sun, Q. Li, Q. Tang, Z. Wu, "Surprisingly advanced CO_2 photocatalytic conversion over thiourea derived gC_3N_4 with water vapor while introducing 200–420nm UV light." Journal of CO_2 Utilization 14 (2016) 143–151.
[34] C. Lei, M. Pi, X. Zhu, P. Xia, Y. Guo, F. Zhang, "Highly efficient visible-light photocatalytic performance based on novel AgI/g-C_3N_4 composite photocatalysts." Chemical Physics Letters 664 (2016) 167-172.
[35] K.S. Sing, "Reporting physisorption data for gas/solid systems with special reference to the determination of surface area and porosity (Recommendations 1984)." Pure and applied chemistry 57 (1985) 603-619.
[36] M. Kruk, M. Jaroniec, "Gas adsorption characterization of ordered organic– inorganic nanocomposite materials." Chemistry of materials 13 (2001) 3169-3183.
[37] I. Papailias, T. Giannakopoulou, N. Todorova, D. Demotikali, T. Vaimakis, C. Trapalis, "Effect of processing temperature on structure and photocatalytic properties of g-C_3N_4." Applied Surface Science 358 (2015) 278-286.
[38] D.R. Paul, R. Sharma, S. Nehra, A. Sharma, "Effect of calcination temperature, pH and catalyst loading on photodegradation efficiency of urea derived graphitic carbon nitride towards methylene blue dye solution." RSC advances 9 (2019) 15381-15391.
[39] F. Hasanvandian, M. Moradi, S.A. Samani, B. Kakavandi, S.R. Setayesh, M. Noorisepehr, "Effective promotion of g–C_3N_4 photocatalytic performance via surface oxygen vacancy and coupling with bismuth-based semiconductors towards antibiotics degradation." Chemosphere 287 (2022) 132273.
[40] T. Giannakopoulou, I. Papailias, N. Todorova, N. Boukos, Y. Liu, J. Yu, C. Trapalis, "Tailoring the energy band gap and edges' potentials of g-C_3N_4/TiO_2 composite photocatalysts for NO_x removal." Chemical Engineering Journal 310 (2017) 571-580.
[41] Q. Shen, C. Wu, Z. You, F. Huang, J. Sheng, F. Zhang, D. Cheng, H. Yang, "g-C_3N_4 nanoparticle@ porous g-C_3N_4 composite photocatalytic materials with significantly enhanced photo-generated carrier separation efficiency." Journal of Materials Research 35 (2020) 2148-2157.
[42] A. Rashidizadeh, H. Ghafuri, Z. Rezazadeh, "Improved visible-light photocatalytic activity of g-C_3N_4/$CuWO_4$ nanocomposite for degradation of methylene blue." Multidisciplinary Digital Publishing Institute Proceedings 41 (2020) 43.
[43] D.-P. Bui, M.-T. Pham, H.-H. Tran, T.-D. Nguyen, T.M. Cao, V.V. Pham, "Revisiting the Key Optical and Electrical Characteristics in Reporting the Photocatalysis of Semiconductors." ACS omega 6 (2021) 27379-27386.
[44] E. Farahi, N. Memarian, "Nanostructured nickel phosphide as an efficient photocatalyst: effect of phase on physical properties and dye degradation." Chemical Physics Letters 730 (2019) 478-484.
[45] S. Khajuee, N. Memarian, "Hydrothermal synthesis of ultrafine SnO_2 nanospheres: effect of reaction time on physical properties." The European Physical Journal Plus 136 (2021) 1-12.
[46] E. Farahi, N. Memarian, "Surfactant-assisted synthesis of Ni_2P nanostructures: effect of surfactant concentration on photocatalytic activity." The European Physical Journal Plus 137 (2022) 463.
[47] M. Sabarinathan, S. Harish, J. Archana, M. Navaneethan, H. Ikeda, Y. Hayakawa, "Highly efficient visible-light photocatalytic activity of MoS_2–TiO_2 mixtures hybrid photocatalyst and functional properties." RSC advances 7 (2017) 24754-24763.
[48] M. Epifani, S. Kaciulis, A. Mezzi, D. Altamura, C. Giannini, R. Díaz, C. Force, A. Genç, J. Arbiol, P. Siciliano, "Inorganic photocatalytic enhancement: activated RhB photodegradation by surface modification of SnO_2 nanocrystals with V_2O_5-like species." Scientific reports 7 (2017) 1-13.
[49] R.V. Eldik, K.A. Connors "Chemical Kinetics: The Study of Reaction Rates in Solution." VCH Verlagsgesellschaft Weinheim New York, ISBN 3-527-28037-5, 480 Seiten, Preis: DM 168,–, Wiley Online Library, (1991).
[50] M. Ahmaruzzaman, S.R. Mishra, "Photocatalytic performance of g-C_3N_4 based nanocomposites for effective degradation/removal of dyes from water and wastewater." Materials Research Bulletin 143 (2021) 111417.
[51] H. Ashiq, N. Nadeem, A. Mansha, J. Iqbal, M. Yaseen, M. Zahid, I. Shahid, "G-C_3N_4/Ag@ $CoWO_4$: A novel sunlight active ternary nanocomposite for potential photocatalytic degradation of rhodamine B dye." Journal of Physics and Chemistry of Solids 161 (2022) 110437.